ARTICLE

PdP/WO₃ Multi-functional Catalyst with High Activity and Stability for Direct Liquid Fuel Cells (DLFCs)

Sachin Kumar[a,b], Roby Soni[c], and Sreekumar Kurungot[a,b,*]

Abstract: Direct liquid fuel cells are the energy conversion devices which utilize formate and methanol as the fuels. These systems are alleviated from the problem of H_2 transport and storage, making them highly desirable for various practical applications. However, the low stability and activity of the carbon supported catalysts such as Pt/C both in the anode and cathode is a critical hindering factor towards their further development. As a practical solution to overcome this issue, in this work, we are reporting on the development of phosphorus-doped palladium (PdP) nanoparticle-supported tungsten oxide (WO_3) nanorods (PdP/WO₃) as a versatile multifunctional catalyst for facilitating the oxidation of formate and methanol in the anode and oxygen reduction reaction (ORR) in the cathode. Strong metal-support interactions and electronic modifications incurred by the doped phosphorus help this system to achieve desirable property characteristics to enable it to effectively function both for the anode and cathode applications. PdP/WO₃ showed 16-times higher mass activity compared to Pt/C even after 3000 start/stop cycles for ORR. For formate and methanol oxidation, PdP/WO₃ exhibited current densities of 0.50 and 0.734 A mg^{-1}_{Pd}, respectively, outperforming the *state-of-the-art* catalysts. With these bifunctional features, PdP/WO₃ stands out as a potential system to be used as an anode and cathode catalyst in direct liquid fuel cells, all the while offering an opportunity for the development of the carbon-free electrocatalysts.

a. *Physical and Materials Chemistry Division, CSIR-National Chemical Laboratory, Dr. Homi Bhabha Road, Pune 411 008, India.*
b. *Academy of Scientific and Innovative Research, Ghaziabad, 201002, India.*
c. *Laboratory for Chemistry and Life Science, Institute of Innovative Research, Tokyo Institute of Technology, 4259, Nagatsuta, Midori-ku, Yokohama 226-8503, Japan.*
*mail for S.K.: k.sreekumar@ncl.res.in.
ORCID Sreekumar Kurungot: 0000-0001-5446-7923
d.

Introduction

Hydrogen (H_2) as the fuel for Polymer Electrolyte Membrane Fuel Cells (PEMFCs) requires sophisticated transportation and storage technologies compared to its conventional liquid-state counterparts. As an alternative to the direct hydrogen-based fuel cells, Direct Formic Acid/Formate Fuel Cell (DFAFC/DFFC) and Direct Methanol Fuel Cell (DMFC), which utilize formic acid/formate and methanol respectively as the liquid fuels, have tremendous potential. Even though these systems can alleviate the problems associated with the H_2 storage and transport, on a kinetic perspective, unlike the very fast oxidation of H_2, the methanol and formate oxidation processes are comparatively sluggish.[1] The slow kinetics of methanol and formate oxidation imposes the use of a highly active catalyst to facilitate the concerned reactions. Pt/C is the most active catalyst for the methanol/formate oxidation, but the CO poisoning of Pt during the operation demands its CO-tolerant alternatives for DFFC/DMFC.[2,3] Pd/C is one of the potential catalysts for carrying out the electrocatalytic oxidation of formic acid/formate and methanol as it is cost-effective, highly active and significantly resistant to CO poisoning.[4] However, Pd supported over the carbon substrates generally show performance degradation during long-term operation due to the potential induced carbon corrosion/dissolution under the working potential window of the systems.[5] Like in the anode of DFFC and DMFC, the carbon corrosion is a serious issue in the cathode of these systems as well since the corrosion resistance of the *state-of-the-art* Pt/C catalysts for ORR is relatively low.

To counter or address the carbon corrosion of the catalysts in the system as a whole, the coupling of the active metals with suitable metal oxides to provide the necessary electronic modulations has been extensively pursued.[6,7,8] The electronic interaction between Pd and the metal oxide not only stabilizes the Pd but it also provides benefits in terms of increased electrochemically active surface area, resistance towards agglomeration, and favorable electronic structural modification of Pd. Therefore, a properly designed catalyst consisting of an appropriate metal oxide supported with Pd nanoparticles has the anticipated potential to evolve as a highly stable electrocatalyst for methanol/formate oxidation. As previously mentioned, since carbon corrosion is a common issue in both the anode and cathode of PEMFC, DMFC, DFFC and DFAFC, replacement of carbon with a suitable metal oxide will provide additional benefits in terms of enhanced durability and reduced carbon footprint. If a Pd-metal oxide-based multifunctional catalyst possessing the ability to catalyze the anode (methanol and formate oxidation) and the cathode (oxygen reduction) can be designed, additional benefits on the cell fabrication process of having a single catalyst based electrode for both the anode and cathode can be achieved. Electrodes for the anode and cathode based on the same catalyst will simplify the electrode fabrication protocols. Also, Pd has half the cost of Pt; therefore, the replacement of Pt with Pd will have significant cost benefits on a device level.

TiO_2 and WO_3 have been extensively explored as the metal oxide support for dispersing different metal nanoparticles. These metal oxides are stable in acidic medium and they exhibit good oxidation resistance. Owing to the earth`s abundance of WO_3 and the intrinsic properties such as hydrogen spillover effect[9,10,11,12], resistance to CO poisoning[13], and strong metal-support interaction (SMSI) effect[14,15], it is regarded as one of the promising supports for the nanoparticles. SMSI effects are well known to enhance the catalytic properties of the supported metal nanoparticle due to the electronic and strain effects. In one report, Pd nanotetrahedron deposited over tungsten oxide ($W_{18}O_{49}$) nanosheets showed enhanced activity for ORR in the alkaline medium.[16] Also, Pd coupled to $WO_{2.7}$ exhibited enhanced stability and activity, which was attributed to the electronic effects and modifications in the lattice parameters of the Pd lattice.[11] For formic acid oxidation, the alloy of PdCu coupled to the $WO_{2.7}$ has demonstrated 2.65 times enhanced activity compared to the uncoupled PdCu.[10] Also, Pd-B-P alloy has shown to exhibit multi-functional activity for the oxidation of ethanol and ethylene glycol, and also for the reduction of oxygen. Nevertheless, these systems need to be further supported over the Vulcan carbon, which limits their utility for long-term operation in the fuel cells. Apart from SMSI and induced electronic modifications in the supported metal nanoparticles, WO_3 is also resistant to corrosion at the high operating voltages of the systems. Thus, WO_3 comes as a promising alternative as a carbon-free support material. Moreover, it is well known that incorporation of non-metals such as B and P in the Pd lattice improves the catalytic activity.[17,18,19,20,21,22] P can be easily incorporated *in-situ* into the Pd lattice using sodium hypophosphite, which acts simultaneously as the reducing agent and a source of P.[23] Incorporation of P in the Pd can help to restrict the size of the nanoparticles of PdP within small range while ensuring their homogenous distribution along the substrate.[24] In addition to these benefits, the incorporated P can induce low-crystallinity in the Pd particles; Pd nanoparticles of low crystallinity are known to have superior specific and mass activities for ORR compared to their crystalline counterparts.[25]

Considering the abovementioned advantages of having WO_3 as a carbon-free support and P as a dopant, in this work, we are introducing PdP nanoparticle-supported WO_3 nanorod (PdP/WO_3) as a multifunctional electrocatalyst for ORR, methanol oxidation and formate oxidation. The electronic properties of the Pd nanoparticles are found to be tuned by incorporating P in the lattice which causes modification in the d-band by inducing strain in the Pd lattice. Also, the developed synthesis strategy for preparing PdP/WO_3 ensured concomitant doping and dispersion of P and Pd, respectively, in a single step. The prepared material has been thoroughly investigated for its unique multifunctional properties for facilitating ORR, methanol oxidation and formate oxidation along with its corrosion resistance characteristics under potential induced conditions.

2.0 Experimental Section

Preparation of the WO₃ nanorod support: WO_3 nanorods were synthesized by the modified procedure presented elsewhere.[26] Briefly, 0.825 mg of sodium tungstate and 0.560 mg of sodium chloride were added to 19 ml of water. Subsequently, the pH of the solution was adjusted to around 2.0. The solution was stirred for 1 h for homogenization and the obtained solution was transferred to a 25 ml hydrothermal autoclave, which was kept at 180-200 °C for 3 h. The product obtained after the hydrothermal treatment was filtered, washed with ethanol and water, and dried at 80 °C for 12 h in an oven. The dried product was further calcined at 400 °C under air atmosphere for 3 h.

Preparation of PdP/WO₃: In order to accomplish the simultaneous doping of P and decoration of 10 wt.% Pd on the WO_3 nanorod, 30 mg of WO_3 nanorod was dispersed in 20 ml of de-ionized water through sonication for 30 min. In the above solution, 10 mg/5 ml of disodium tetrachloropalladate (Na_2PdCl_4) was added and sonicated for 30 min., followed by overnight stirring. To this mixture, 0.106 g of sodium hypophosphite and 0.113 g of sodium borohydride were added drop-wise. Afterwards, PdP/WO₃ was obtained through filtration and washing with water and ethanol. The obtained PdP/WO₃ was dried overnight at 80 °C

Preparation of Pd/WO₃: To prepare Pd/WO₃ composite containing 10 wt.% loading of Pd, the abovementioned procedure for the preparation of PdP/WO₃ was followed except for the addition of sodium hypophosphite.

Electrochemical Characterization: For the electrochemical characterization of the catalyst for formate oxidation, methanol oxidation and oxygen reduction reaction, a slurry was prepared by dispersing 5 mg of PdP/WO₃ in a mixture of 1.0 ml each of water and ethanol through sonication. Subsequently, 20 µl of the slurry was drop-coated on the glassy carbon rotating disc electrode (RDE) (geometric area of 0.196 cm²) as the working electrode (WE), and dried under an IR lamp. Comparatively, the surface area of the WO_3 was lower than that of the Vulcan carbon/carbon black.[37] The electrodes based on WO_3 were prepared by directly coating the ink of the respective catalysts, without adding any ionomer, on the electrode. However, the Pd/C (10 %) and Pt/C (20 %) slurries were prepared by sonicating 5 mg of the catalyst in a mixture of 0.75 ml of DI water and 0.25 ml of isopropyl alcohol along with 20 µl of Nafion as a binder. For the analysis, 10 µl of the slurry was drop-coated on the glassy carbon surface of the rotating disc electrode (RDE), and subsequently dried under an IR lamp. For evaluating the methanol and formate oxidation activities of the different catalysts, the corresponding electrochemical tests were performed in an electrolyte containing 0.1 M KOH + 1.0 M

methanol and 0.3 M KOH + 0.1 M formic acid, respectively. On the other hand, evaluation of the ORR activity was performed in 0.1 M KOH solution. Hg/HgO was used as the reference electrode (RE) and a graphite rod was employed as a counter electrode. All the potential values are converted to the V *vs* RHE scale using the equation E(RHE) = E(Hg/HgO) + 0.878 V (Figure S1). All electrochemical experiments were performed on a Biologic potentiostat (SP-300) in combination with a Pine RDE/RRDE unit.

Carbon Corrosion: For studying carbon corrosion, a start-stop cycle was performed by scanning the potential in the range of 1.0 to 1.5 V (scan rate: 100 mV/s) under nitrogen-enriched conditions for 3000 cycles and comparing the results before and after the cycles. The mass activity of the catalysts for oxygen reduction reaction was calculated using the kinetic current density (j_k) at 0.90 V. The j_k value corresponding to a potential of 0.90 V was computed using the K-L equation i.e., $\frac{1}{j} = \frac{1}{j_d} + \frac{1}{j_k}$, or $j_k = \frac{j_d \times j}{j_d - j}$, where j is the observed current density, j_d is the limiting current density, and j_k is the kinetic current density. The mass activity was calculated using j_k normalized to the mass of the active component (Pt/Pd) in the system. For methanol oxidation, the mass activity was obtained by normalizing the peak current to the active mass component (Pd/Pt). A long-term stability test of PdP/WO₃ was carried out by potential cycling within a potential range of 0.0 to 1.2 V in N_2 saturated 0.1 M KOH and 1.0 M methanol for 1000 cycles. For formate oxidation, the mass activity was obtained by normalizing the obtained current at 0.60 V to the active mass component. A long-term stability test of PdP/WO₃ was carried out by potential cycling within a potential range of 0.0 to 0.80 V in N_2 saturated 0.3 M KOH and 0.1 M formic acid for 1000 cycles.

Physical Characterization X-ray diffraction (XRD) analysis was performed on a PANalytical X'Pert PRO instrument. Field emission scanning electron microscopy (performed on FEI Nova Nano SEM 450) and transmission electron microscopy (carried out on FEI TECNAI G2 F20 instrument) analyses were performed to gain information related to the morphological features of the prepared materials. A Quanta 2003D FEI instrument in combination with a TEAM TM EDS analysis system was used for performing the energy dispersive X-ray spectroscopy (EDS) elemental mapping and a JEM-F200 instrument was used for performing the HAADF-STEM analysis. For examining the electronic properties of the different catalysts, X-ray photoelectron spectroscopy (XPS) was carried out on the Thermo Scientific K-Alpha + machine with a fully integrated monochromated small-spot X-ray photoelectron spectrometer (XPS) system.
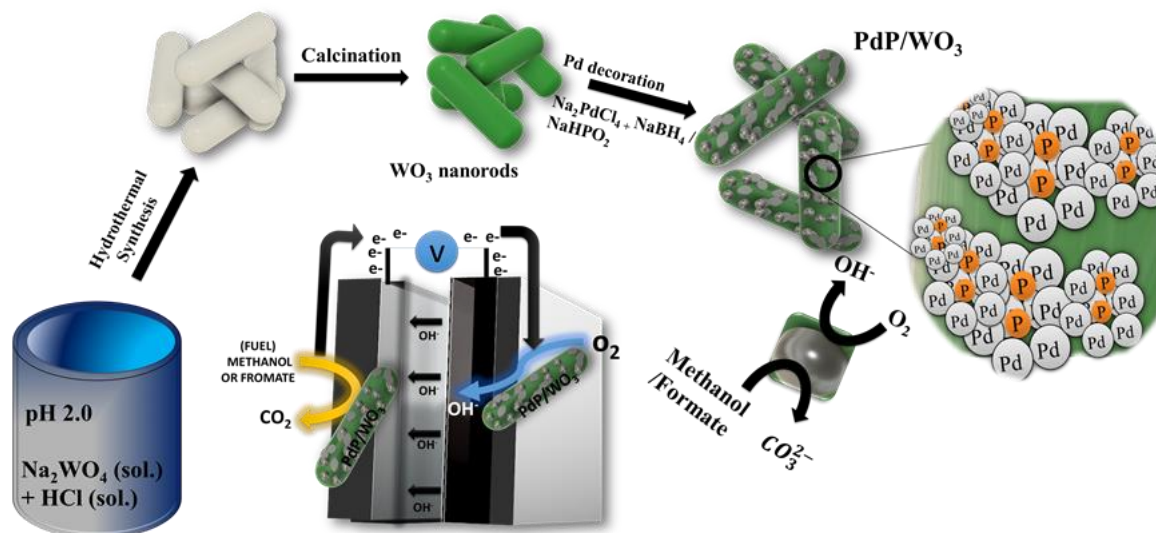
Scheme 1. Schematic representation of the various steps involved in the synthesis of PdP/WO₃ and its application as an electrocatalyst for facilitating both oxidation of methanol/formate and reduction of oxygen.

3.0 Results and Discussion

Scheme 1 shows the graphical representation of the procedure ivolved in the synthesis of PdP/WO₃ nanorod catalyst and its utilization as an electrocatalyst for facilitating ORR and methanol/formate oxidation. Firstly, the WO₃ nanorod was prepared through the hydrothermal method, which was then calcined to obtain a more crystalline, and a greenish-white powder indicating the creation of the oxygen vacancies. These types of surface defects in the metal oxides are known to subsequently lead to the improvement in the properties such as the charge transference.[27] Afterward, P-doped Pd nanoparticles were deposited on WO₃ through a colloidal method in a single step. Sodium hypophosphite added here acts as the reducing agent as well as the source of P. The mechanism of the P incorporation into the Pd matix is shown below[28]:

$$Pd^{2+} + H_2PO_2^- \rightarrow Pd + H_3PO_3^-$$
$$H_2PO_2^- + H^- \rightarrow H_2O + H_2 + P$$
$$nPd + P \rightarrow Pd_nP$$
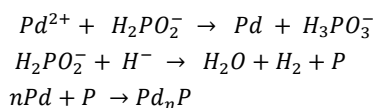
To understand the crystal structure of the synthesized WO₃ and P-doped Pd nanoparticle-deposited WO₃ (PdP/WO₃), XRD analysis was performed; the corresponding data is shown in **Figure 1**. In the figure, the diffraction peaks corresponding to the 2θ values of 23.03, 24.46, 27.04, 28.34, 33.78, 63.93, 47.11, 49.83 and 56.14° are indexed to the (001), (110), (101), (200), (111), (201), (002), (220), and (202) planes of the hexagonal phase of WO₃, which has been confirmed with the JCPDS Card No. 00-033-1387. Pd(111) peak in PdP/WO₃, Pd/WO₃, and Pd/C appear at 39.85, 40.07, and 40.46°. The P doping in PdP/WO₃ shifts the Pd (111) plane by 0.22° and 0.61° negatively compared to Pd/WO₃ and Pd/C, respectively, which indicates expansion in the Pd lattice. This lattice expansion can be explained in terms of the P-doping. Interestingly, we also find that WO₃ does influence the Pd lattice; we observed a negative shift of 0.39° in the case of Pd/WO₃ compared to Pd/C, which conforms with the other literature reports also, where the lattice expansion was observed for the supported Pd nanoparticles.[11] The low 2θ value of Pd (111) in the case of PdP/WO₃ compared to that of Pd/WO₃ and Pd/C indicates crystal expansion of the Pd lattice which can be attributed to the incorporation of P in the Pd crystal.[29] Since P is non-metallic and smaller in size compared to Pd, this size difference can induce strain in the crystal, resulting in crystal expansion.[30,11,] The lattice expansion is well known for having an effect on the d-band bandwidth, which tune the catalytic activity.[31,] It has been reported that there is a significant reduction in the oxidation current of formic acid due to lateral compression of the Pd (111) plane while more open Pd monolayer shows high catalytic activity towards the reaction.
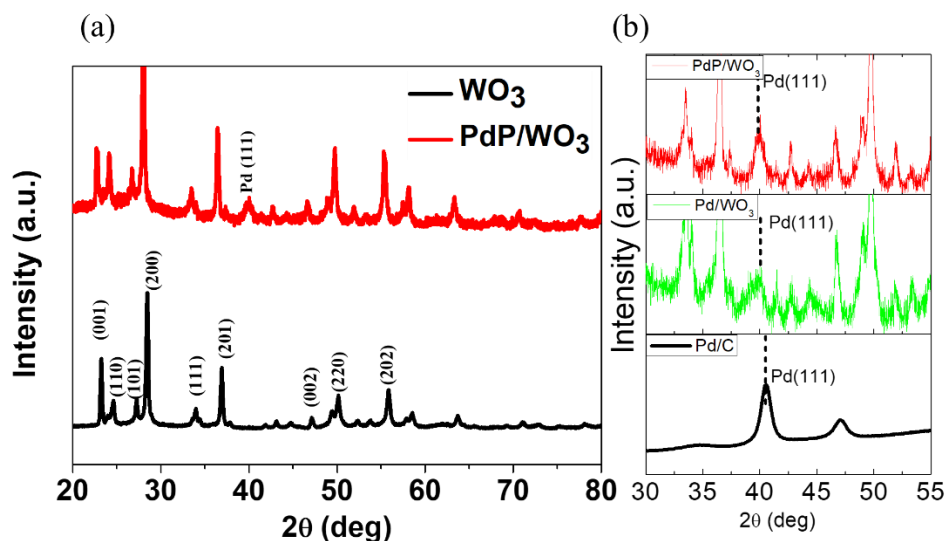
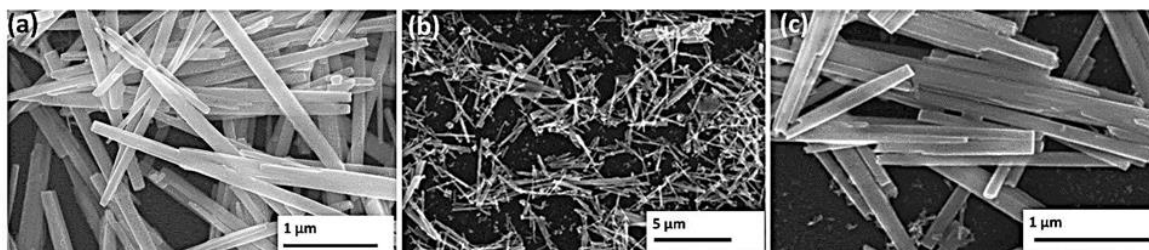Figure 1. Comparative XRD patterns of (a) WO₃ nanorod and PdP coupled WO₃ nanorod (PdP/WO₃) and (b) Pd/C, Pd/WO₃ and PdP

Figure 2. FESM images of (a) WO₃ calcined at 400° C and (b)-(c) PdP/WO₃.

Morphology of the WO₃ was observed by recording FESEM images, which are presented in **Figure 2a**. It can be seen from **Figure 2a-c** that both WO₃ and PdP/WO₃ have acquired nanorod-like morphology. Further, the EDS elemental mapping of PdP/WO₃ shows the presence of the Tungsten (W), Oxygen (O), Palladium (Pd), and Phosphorous (P) (**Figure S2)**. The EDS data thus stands out as a proof for P doping and supplements the XRD data, which provided a strong evidence for the lattice expansion of Pd in PdP/WO₃ caused by the intervention of the doped P. Also, the elemental analysis clearly shows the even distribution of the doped P in PdP/WO₃ and thus confirms the homogeneous coexistence of Pd and P in effectively facilitating the synergistic modulations mobilized by the electronic interactions between the systems.

To gain more insightful information on the mosphological characteristics of the system, TEM analysis of WO₃ and PdP/WO₃ was performed. As can be seen in **Figure 3a** and **b**,

WO₃ nanorods display a highly smooth surface with the diameter ranging from 50-100 nm. The images given in **Figure 3c-e** represent the TEM images recorded for the PdP/WO₃ composite at three different magnifications. A fairly homogenious distribution of the PdP nanoparticles without any indication of agglomeration on the surface of the WO₃ nanorods is the key feature of the PdP/WO₃ system as revealed from the TEM images. Achieving an aggregation-free dispersion of metallic nanoparticles on an oxide substrate like WO₃ is challenging especially when the size of the active components needs to be restricted within few nanometers. Achieving such type of particle distribution will essentially enable the material to attain high electrochemically active surface area and subseqently improved performance in the targeted electrochemkcal processes. The size of the PdP nanoparticles measured from the TEM images is within the range of 4-5 nm. It should be noted that, as per some previouss reports, a particle size in the range of 5-7 nm is found to be favoring the electro-

oxidation of the formic acid through the direct pathway leading to the CO_2 generation without the intermediate pathway resulting into CO generation.[32] These advantages can be related in terms of the sufficient availability of the $-OH_{ads}$ species on the surface of the Pd particles, which act as intermediates for completing the CO oxidation process.

Morphology of the WO_3 was observed by recording FESEM images, which are presented in **Figure 2a**. It can be seen from **Figure 2a-c** that both WO_3 and PdP/WO_3 have acquired nanorod-like morphology.   Further, the EDS elemental mapping of PdP/WO_3 shows the presence of the Tungsten (W), Oxygen (O), Palladium (Pd), and Phosphorous (P) (**Figure S2)**. The EDS data thus stands out as a proof for P doping and supplements the XRD data, which provided a strong evidence for the lattice expansion of Pd in PdP/WO_3 caused by the intervention of the doped P. Also, the elemental analysis clearly shows the even distribution of the doped P in PdP/WO_3 and thus confirms the homogeneous coexistence of Pd and P in effectively facilitating the synergistic modulations mobilized by the electronic interactions between the systems.

To gain more insightful information on the mosphological characteristics of the system, TEM analysis of WO_3 and PdP/WO_3 was performed. As can be seen in **Figure 3a** and **b**, WO_3 nanorods display a highly smooth surface with the diameter ranging from 50-100 nm. The images given in **Figure 3c-e** represent the TEM images recorded for the PdP/WO_3 composite at three different magnifications. A fairly homogenious distribution of the PdP nanoparticles without any indication of agglomeration on the surface of the WO_3 nanorods is the key feature of the PdP/WO_3 system as revealed from the TEM images. Achieving an aggregation-free dispersion of metallic nanoparticles on an oxide substrate like WO_3 is challenging especially when the size of the active components needs to be restricted within few nanometers. Achieving such type of particle distribution will essentially enable the material to attain high electrochemically active surface area and subseqently improved performance in the targeted electrochemkcal processes. The size of the PdP nanoparticles measured from the TEM images is within the range of 4-5 nm and particles also shows the interconnected features. It should be noted that, as per some previouss reports, a particle size in the range of 5-7 nm is found to be favoring the electro-oxidation of the formic acid through the direct pathway leading to the CO_2 generation without the intermediate pathway resulting into CO generation.[32] These advantages can be related in terms of the sufficient availability of the $-OH_{ads}$ species on the surface of the Pd particles, which act as intermediates for completing the CO oxidation process.
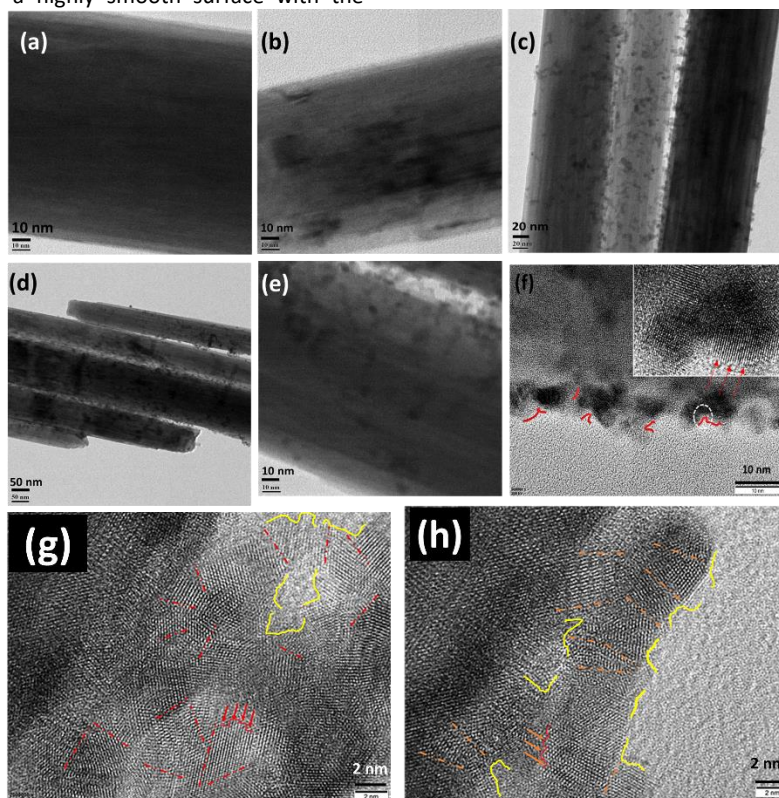

Figure 3. TEM images of the bare WO_3 (a and b) nanorods and PdP/WO_3 (c-e) showing the distribution of the PdP nanoparticles on the surface of the WO_3 nanorods; (f-h) HR-TEM images of PdP/WO_3 showing the kinks (marked by the red curved line) and the inset representing the step edges (marked by the red arrows).

6

Further, kinks, steps, and edges of PdP can be seen in the HRTEM images ; the kinks and steps are marked with the red curved lines while the step atoms are marked by the red arrows (**Figure 3f-h & Figure S3**). These kinks and edges possess atoms in the lower coordinating states, which are known to be displaying enhanced activity compared to the smooth surfaces.[33] Undercoordinated surfaces are of high surface energy, enabling them to exhibit high catalytic activity. Further, the grain boundaries formed by the interweaving of the crystallites are also observed in the HR-TEM images (inset of **Figure 3f**); these grain boundaries contribute to the creation of the overall defects in the nanoparticles. The high density of these defects is known to improve the electro-catalytic activity due to the open coordinated nature of the atoms.[34] Atomic defects create more exposed step atoms, which concomitantly help to redefine the intrinsic activity characteristics and is being practiced as an effective strategy to fine tune performance of the catalysts for specific applications .[35] Previously, the XRD results indicated that the incorporation of P in the Pd crystal causes the lattice expansion with the introduction of strain in the lattice.

To gain more insightful information on the electronic modification, surface electronic structure and the effect of WO_3 on the electronic properties of the supported nanoparticles, XPS analysis was performed on PdP/WO_3, PdP/C, and WO_3; the corresponding data is shown in **Figure 4**. The XPS survey spectra of PdP/WO_3, Pd/WO_3, PdP/C and WO_3 given in **Figure 4a** clearly show the signatures corresponding to the presence of W, O, Pd and P. Moreover, to get a better understanding of the effect of WO_3 support on inducing the electronic structure modification of the supported PdP nanoparticles, we compared the XPS core spectra of Pd 3d in PdP/WO_3 and its Vulcan carbon supported counterpart, *viz*., PdP/C (**Figure 4b**). A shift in the electron binding energy of Pd 3d toward the lower energy region has been observed in the case of PdP/WO_3 and Pd/WO_3 compared to that in PdP/C. The Pd 3d peaks for PdP coupled to Vulcan carbon in PdP/C appear at 341.64 and 336.14 eV for the $Pd_{3/2}$ and $Pd_{5/2}$ states, respectively, whereas, the corresponding states in the case of the WO_3 supported system (PdP/WO_3) appear respectively at 339.68 and 334.38 eV. Similarly, in case of Pd/WO_3, the binding energies for $Pd_{3/2}$ and $Pd_{5/2}$ appear at 339.92 and 334.52, respectively. The shift in the Pd 3d binding energies indicates the existence of strong electronic interaction between Pd and WO_3, where the lower binding energy of the PdP and Pd supported on WO_3 indicates charge transfer from WO_3 to the Pd nanoparticles.[36] This shift can be further substantiated by the changes in the binding energies of the W and O.[37] The binding energies of W $4f_{5/2}$ and W $4f_{7/2}$ are 37.26 and 35.16 eV, respectively, **(Figure 4c)** in WO_3, which increased respectively to 37.63 and 35.43 eV, again inferring to the strong electronic interactions operating between the WO_3 and PdP nanoparticles.

Similarly in case of Pd/WO_3, the binding energy values appear at 37.60 and 35.4 eV for W $4f_{5/2}$ and W $4f_{7/2}$, respectively. The comparative O 1s core spectra of WO_3 and PdP/WO_3 presented in **Figure 4d** indicate that the binding energy for the O 1s in WO_3 is 529.46 eV compared to 530.33 and 530.2 eV recorded in the case of PdP/WO_3 and Pd/WO_3, respectively. Here, an increase in the binding energy of O in PdP/WO_3 and Pd/WO_3 is possible by the electron density transfer from the support material to the PdP nanoparticles. This is in conformity with the other metal oxides, which showed similar effects.[37] XPS of P 2p measured in PdP/WO_3 is given in **Figure 4e**; the binding energy indicates that the P at the surface is mostly in the oxidized form. The binding energy recorded at 129.73 eV confirms the presence of the P in the metallic state, which further substantiates with the XRD findings, while that recorded at 133.93 eV is ascribed to the P in the oxidized state.[38]

From the mechanistic point of view, the negative alternation in the binding energy exhibits a low barrier for the O_2 dissociation and thus increases the catalytic activity for oxygen reduction (**Figure S4. a**).[39] In the case of methanol and formate, hydroxide(ads.) moieties (OH-(ads)) facilitate the electrochemical oxidation of the methanol and formate (**Figure S4. a** & **b**). Thus, in addition to the adsorption of the reactant and intermediates, the increased presence of OH-(ads) on the Pd surface enhances the electrochemical oxidation of the methanol and formate. Sufficient hydroxyl ions are necessary for the dehydrogenation of the methanol and formate which promotes the electrochemical oxidation of the formate and methanol. Therefore, increased concentration of OH-(ads) on the Pd surface enhances the electrochemical oxidation of the methanol and formate. Hydroxyl ions are required to remove the hydrogen instantly.[40] Hence, negative alternation of the binding promotes the adsorption of the hydroxyl ion on the Pd surface, which subsequently enhances the methanol oxidation and formate oxidation reactions. This enhanced hydroxyl adsorption can be explained in terms of the d-band center modulation. The d-band center influences the OH- adsorption on the Pd surface. Higher d-band center adsorbs hydroxyl ion less strongly than the substrate with lower d-band center.[41]

The detailed physical characterization as given in the previous sections provided valid evidences on the electronic modulations incurred by PdP/WO_3 as a result of the synergistic effects originated from the metal-support interaction and the effect of the doped P in the Pd crystallites. A favorable interplay of such electronic modulations and synergetic interactions can induce significant influence on promoting the electrocatalytic activity of the system. To get insights on such activity modulations, the system has been investigated for electrochemical reduction of oxygen, followed by oxidation of methanol and formic acid. The electrochemical oxygen reduction reaction (ORR) has been performed in 0.1 M KOH; the corresponding
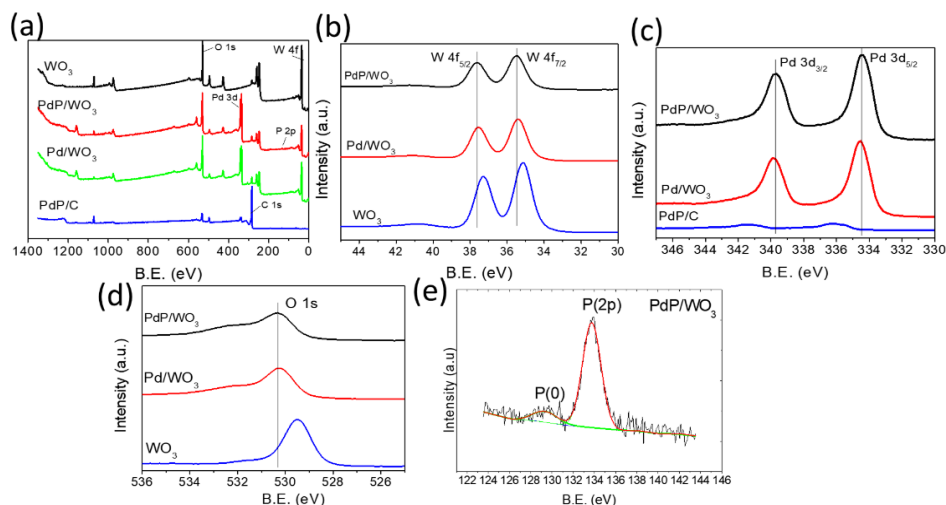
7

Figure 4. (a) XPS survey spectra of PdP/WO$_3$, Pd/WO$_3$, PdP/C and WO$_3$, (b) comparative XPS core spectra of Pd 3d in PdP/WO$_3$, Pd/WO$_3$ and PdP/C; (c) comparison of PdP/WO$_3$,Pd/WO$_3$ and the pristine WO$_3$ nanorods with respect to the energy changes in the W 4f spectra; (d) O1s XPS core spectra of WO$_3$, Pd/WO$_3$and PdP/WO$_3$; (e) P 2p spectrum of PdP/WO$_3$.

cyclic voltammograms (CVs) recorded under N$_2$ and O$_2$ saturated conditions for PdP/WO$_3$ and Pt/C are presented in **Figure 5a** and **b**, respectively. The CVs recorded in the O$_2$ saturated electrolyte show a sharp increase in the current unlike the N$_2$ saturated condition, indicating the ORR activity of the systems when the electrolyte facilitates O$_2$ supply to the active sites. A more insightful information on the intrinsic ORR activity characteristics of the systems can be gained from the recorded comparative linear sweep voltammograms (LSVs) as presented in **Figure 5c**. A comparison between PdP/WO$_3$, Pd/WO$_3$, Pd/C and Pt/C indicates that PdP/WO$_3$ with its onset potential of 1.04 V and a half-wave potential (E$_{1/2}$) of 0.91 V outperformed both Pt/C (1.0 and 0.84 V, respectively), Pd/C (0.97 V and 0.78 V, respectively) and Pd/WO$_3$ (1.03 V and 0.905 V). This corresponds to 60, 120 and 5 mV reduction in E$_{1/2}$ for PdP/WO$_3$ in comparison to Pt/C, Pd/C and Pd/WO$_3$, respectively, implying to better intrinsic ORR activity incurred by PdP/WO$_3$**.** The mass activity comparison shows that PdP/WO$_3$ exhibits a performance of 1.50 A mg^{-1} compared to Pd/WO$_3$ (1.40 A mg^{-1}), Pd/C (0.11 A mg^{-1}) and Pt/C (0.11 A mg^{-1}) as shown in **Figure S5**. The experimental error bar corresponding to the mass activity at 0.90 V is shown in **Figure S6**. Cyclic Voltammograms for the ECSA calculation is shown in **Figure S7**. The ECSA of Pd has been calculated by using the equation: $\text{ECSA} = \frac{Q_h}{424x \text{ Pd loading}}$, where 424 µC cm^{-2} is the charge associated with the PdO monolayer reduction. ECSA values of PdP/WO$_3$, Pd/WO$_3$ and Pd/C are found to be 36.84 m^{2}g$_{Pd}^{-1}$, 13 m^{2}g$_{Pd}^{-1}$ and 44 m^{2}g$_{Pd}^{-1}$ respectively. While, the ECSA value of Pt has been calculated using the equation: $\text{ECSA} = \frac{Q_h}{210 \text{ x Pt loading}}$, where 210 µC cm^{-2} is the charge associated with hydrogen desorption, ECSA of Pt/C is found to be around 56 m^{2}g$_{Pt}^{-1}$. The enhanced ECSA value of PdP/WO$_3$ compared to Pd/WO$_3$ clearly shows the influence of the P doping in PdP/WO$_3$, having a much more exposed site of Pd. This favorable

activity modulation can be explained in terms of the modification of the d-band center caused by the slight electron density shift from WO$_3$ to the PdP nanoparticles and incorporated P, as evidenced from the XPS analysis.[42,43,44] An increment in the electron density on PdP will cause increase in the orbital occupancy of the d-shell of Pd, leading to the lowering of the d-band center of Pd and favorable tuning of the binding energy of the interacting oxygen and formed reaction intermediates.[45,46] The excess electron density on Pd in PdP/WO$_3$ will subsequently lead to the weakening of the Pd-O bonding. This favors dissociation of the O from the Pd surface, assisting PdP to display enhanced ORR activity.[39] This is further benefited from the P doping in the Pd by creating low coordination sites along the defects created on the kinks and edges, as shown by the HR-TEM analysis.[47]

As a means to understand the kinetics followed for the oxygen reduction, the number of electrons involved (n) in the process has been deduced by generating the Koutecky Levich plots (K-L plots) (**Figure 5d**). This involves plotting of the inverse of both the current density (1/*j*) and angular frequency of rotation ($\omega^{-1/2}$). In this plot, *j* is related to the diffusion limiting current density (*j$_d$*) and kinetic current density (*j$_k$*) through the equation $\frac{1}{j} = \frac{1}{j_d} + \frac{1}{j_k}$. Here, *j$_d$* = *0.62nFAD$^{2/3}v^{-1/6}$ω$^{1/2}C_{O2}$,* where *n* is the number of electron transfer, F is the Faraday's constant (96500 C), A is the electrode area (0.196 cm^2), *D* is the diffusion coefficient of O$_2$ in 0.1M HClO$_4$, *v* is the kinematic viscosity of the electrolyte, *ω* is the angular frequency of rotation and *C$_{O2}$* is   the concentration of the molecular oxygen   in the electrolyte in 0.1 M HClO$_4$. In the present case, a straight line was obtained from the plot of 1/*j* *vs* ω$^{-1/2}$ from which the number of electrons (*n*) involved in ORR could be deduced from the slope of the corresponding plots generated at different potentials.[48] The measured 'n' value confirms the

8

involvement of 4 electrons in the process, inferring to the formation of H_2O as the reduction product.

A further quantifiable performance indicator in understanding the intrinsic ORR activity is the Tafel slope, which can be obtained by plotting the log j (current density) *vs* voltage (V) under the extremely low current polarized conditions (**Figure 5e**). The Tafel slopes measured are 56, 52, 110 and 61 mV dec^{-1} for PdP/WO$_3$, Pd/WO$_3$ Pt/C and Pd/C, respectively. The distinct difference in the Tafel slope values for PdP/WO$_3$ and Pt/C indicates the different mechanisms involved for ORR on these two systems. A low value of Tafel slope in the case of PdP/WO$_3$ points towards faster reaction kinetics on this system compared to Pt/C.

Along the desired 4-electron reduction pathway for ORR leads to water as the final product, the involvement of the parasitic 2-electron reduction process giving H_2O_2 as an undesirable byproduct is a possibility in the case of the ORR catalysts. Along with the active sties, the substrate also can contribute towards such side reactions. Hence, as a means to more precisely quantify both the number of electrons transferred and the amount of H_2O_2 produced during the reduction process, rotating ring disk electrode (RRDE) analysis was performed. Accordingly, **Figure 5f** represents the ring and disk electrode polarization plots as a function of the applied voltage recorded for Pd-P/WO$_3$. The % of H_2O_2 and the number of electrons involved in the reduction process (***n***) were evaluated using the equations $H_2O_2 = \frac{200}{n} I_r / (I_d + \frac{I_r}{0.37})$ and n = $4I_d / (I_d + \frac{I_r}{0.37})$, respectively, where I_r is the ring current, I_d is the disk current and 0.37 is the collection efficiency.
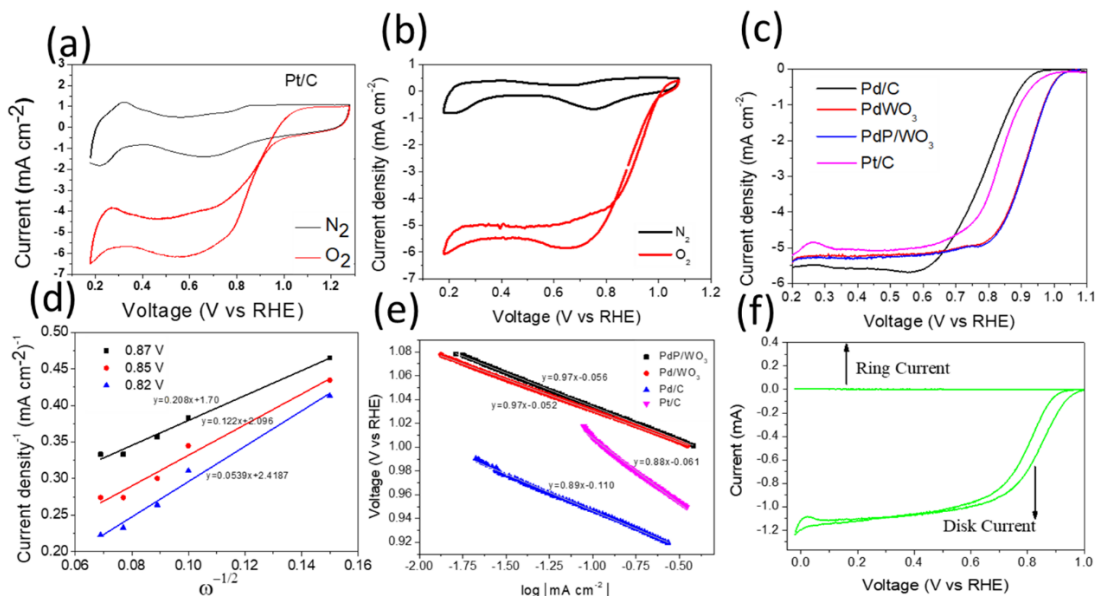

Figure 5. Electrochemical analysis for the oxygen reduction reaction: (a-b) the CV profiles recorded for PdP/WO$_3$ and Pt/C, respectively, in N$_2$ and O$_2$ saturated 0.1 M KOH at a scan rate of 50 mV sec^{-1}, (c) comparative LSV profiles recorded for Pt/C, Pd/WO$_3$, PdP/WO$_3$ and Pd/C at a scan rate of 10 mV sec^{-1} and a rotation speed of 1600 rpm of the working electrode, (d) the Kotuchey-Levich (K-L) plots recorded at different potentials for PdP/WO$_3$, (e) the Tafel plots constructed for Pt/C, Pd/C, Pd/WO$_3$ and PdP/WO$_3$, and (f) the RRDE ring and disk electrode polarization plots recorded for Pd-P/WO$_3$.
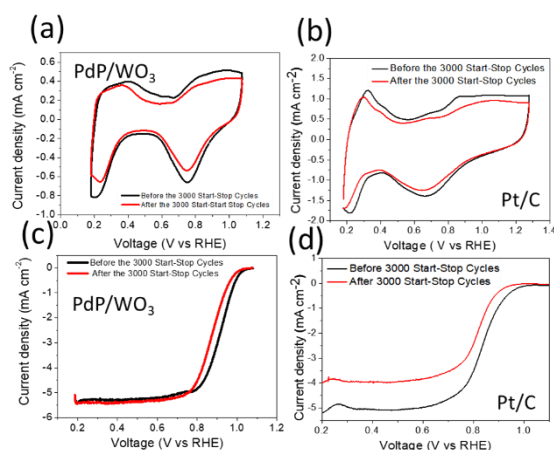
9

ARTICLE

Figure 6. (a) Comparative CV profiles for PdP/WO$_3$ recorded before and after the 3000 start-stop cycles at a scan rate of 50 mV sec^{-1}; (b) comparative CV profiles for Pt/C before and after the 3000 start-stop cycles recorded at a scan rate of 50 mV sec^{-1}; (c) comparative LSV profiles for PdP/WO$_3$ recorded before and after the 3000 start-stop cycles, and (d) comparative LSV profiles for Pt/C recorded before and after the 3000 start-stop cycles.

The RRDE study confirms the dominance of the 4-electron ORR process for both Pt/C and PdP/WO$_3$ with the estimated H$_2$O$_2$ percentages of only 1.7 and 2.1 %, respectively (**Figure S8**).

In addition to the high catalytic activity, an ideal catalyst should be resistant to corrosion in the alkaline environment encountered in the direct liquid fuel cells. The corrosion of the support material has been a prevailing issue that limits long-term operation of the carbon-supported electrocatalysts. To validate the comparative corrosion characteristics of PdP/WO$_3$ and Pt/C, a start-stop cycle has been performed by cycling the potential in the region of 1.0 to 1.5 V (scan rate: 100 mV/s) under nitrogen enriched conditions considering the fact that the corrosion of the support material is higher in this potential range. Initially, full CV and LSV were recorded before the 3000 cycles. Subsequently, start-stop cycles was performed and the CV and LSV were recorded once more to understand the shift in the basic characteristics under the triggered conditions. [49] Figure 6a and b show the CV profiles of PdP/WO$_3$ and Pt/C, respectively, recorded before and after the 3000 start-stop cycles. The benefit of having the carbon-free support in terms of its expected high corrosion resistance can be visualized by comparing the LSV profiles of PdP/WO$_3$ and Pt/C recorded before and after start-stop cycles; the corresponding voltammograms are presented in Figure 6c and d, respectively. The onset potential and E$_{1/2}$ for PdP/WO$_3$ are observed at 1.04 and 0.91 V, respectively, while E$_{1/2}$ was found to be dropped to 0.875 V, subsequent to the start-stop cycles. On the other hand, in the case of Pt/C, the onset and E$_{1/2}$ values of 1.02 and 0.84 V, respectively, measured before the commencement of start-stop

cycles have been dropped to 0.98 and 0.82 V after the test. This means that, the Pt/C system incurred a shift in

Table 1. Comparison of the electrochemical characteristics measured for the different catalysts during the methanol oxidation reaction.

Sample	Peak Current Potential (V)	Peak Current density (A mg^{-1}$_{Pt/Pd}$)	Onset Potential (V vs. RHE)
Pd/C	1.23	612	0.56
Pt/C	1.23	590	0.54
Pd/WO$_3$	1.03	505	0.55
PdP/WO$_3$	1.22	734	0.54

E$_{1/2}$ by 20 mV compared to 35 mV observed for E$_{1/2}$ in the case of PdP/WO$_3$. The shift in the E$_{1/2}$ of Pt/C is slightly lower than that of PdP/WO$_3$, but the observed lower current density (**Figure 6.d**) indicates the poorer performance of Pt/C for oxygen reduction, which might be due to the loss of carbon resulting in Pt detachment from the carbon surface.[50,51] The observed value are much promising, considering the cycling stability of the Pd and Pt in the potential region of 1.0 to 1.5 V. This is especially important considering the fact that the standard reduction potential value of Pd (E^o = 0.951) is much lower than that of Pt (E^o = 1.18).[52] Due to this, the potential window of 1.0 to 1.5 V is expected to make Pd much more susceptible to dissolution compared to the Pt. The superior performance observed here indicates the better structural endurance attained by PdP/WO$_3$ due to the cooperative interactions operating in the system as detailed in the previous sections and lower corrosion rate with WO$_3$ as the carbon-free substrate.

Further, the activity loss has been quantified by representing in terms of the mass activity (**Figure S9**) of the catalysts corresponding to before and after the start-stop cycles using the kinetic current density (j_k) . The j_k value at a potential of 0.90 V was calculated using the K-L equation i.e. $\frac{1}{j} = \frac{1}{j_d} + \frac{1}{j_k}$, or $j_k = \frac{j_d \times j}{j_d - j}$, where j is the observed current density, j_d is the limiting current density, and j_k is the kinetic current density.[53] The mass activity was calculated using j_k normalized to the mass of the active component (Pt/Pd) in the system. The mass activities calculated for PdP/WO$_3$ and Pt/C before the start-stop cycles are ~ 1.5 A mg$_{Pd}$$^{-1}$ and ~ 0.114 A mg$_{Pt}$$^{-1}$ at 0.90 V, respectively. The 13 times higher mass activity recorded for PdP/WO$_3$ is expected to be originated from the favorable activity modulations achieved from the lattice strain effects and the electronic modifications which resulted into the shift in the d-band center. After the start-stop cycles, the mass activity of PdP/WO$_3$ and Pt/C are found to be decreased to ~ 0.596 A mg$_{Pd}$$^{-1}$ and 0.037 A mg$_{Pt}$$^{-1}$ at 0.90 V, respectively, which corresponds to a 16 times lower

performance for Pt/C compared to PdP/WO$_3$. The high loss of mass activity in the case of Pt/C after the cycling, as mentioned before, can be attributed to the detachment and agglomeration of Pt caused by the carbon corrosion. On the other hand, PdP/WO$_3$ shows better retention in mass activity compared to Pt/C. These results indicate the corrosion-resistant properties of WO$_3$ and its applicability as an efficient support material for ORR electro-catalysts. TEM images recorded before and after the durability test are shown in **Figure S10.** The TEM images of Pt/C before and after the test clearly show the agglomeration of the nanoparticles and particle detachment from the carbon support **Figure S10. (a-d)**. While in the case of PdP/WO$_3$, interestingly, we observed that Pd forms an extended interconnected network of Pd nanoparticles instead of the agglomeration (**Figure S10. (e-h))**. This interconnected network of Pd is known to have enhanced performance for electrochemical oxidation of formic acid and methanol oxidation.[54,28] This structural modulation may be explained in terms of the Pd interaction with the support. This clearly shows the influence of the substrate on the stability of the particles.
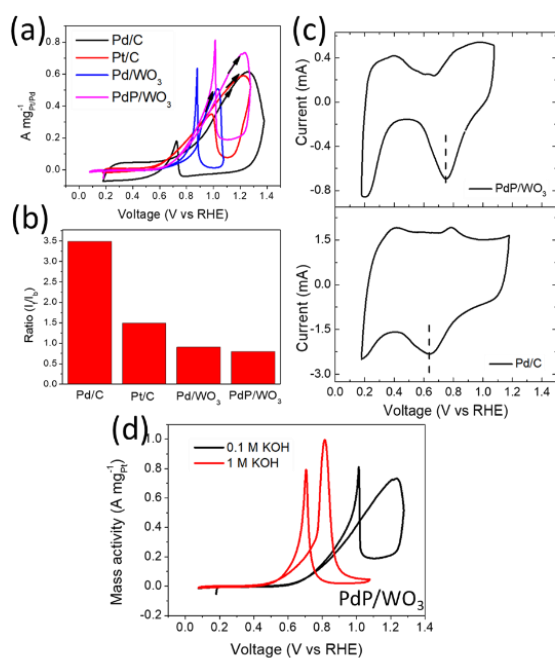

Figure 7. Electrochemical study of the different catalysts for methanol oxidation: (a) CV profiles recorded at a scan rate of 50 mV/s in 1.0 M methanol + 0.1 M KOH, (b) the plot representing the ratio of the forward current density to the backward current density recorded on the different catalysts, (c) CV profiles corresponding to the reduction of the Pd-O peaks recorded for Pd/C and PdP/WO$_3$ in 0.1 M KOH at a scan rate of 50 mV/sec, and (d) CV corresponding to methanol oxidation in 1.0 M methanol + 1.0 M KOH and 0.1 M KOH and 1.0 M KOH for PdP/WO$_3$.

We found out the influence of methanol on ORR by recording LSV profiles in 0.1 M KOH and 1.0 M methanol at a scan rate of 10 mV sec^{-1}in an O$_2$ saturated environment (**Figure S11**). The catalyst is found to be active for oxygen reduction, but with a shift in the onset potential by ~ 100 mV in the presence of methanol.

Since PdP/WO$_3$ is found to be highly resistant against carbon-corrosion, the catalyst has been further explored for its applicability

for methanol and formate oxidation reactions. The methanol oxidation performance of PdP/WO$_3$, Pt/C, Pd/C, and Pd/WO$_3$ has been mapped in 1.0 M methanol containing 0.1 M of KOH and the CV profiles were recorded at a scan rate of 50 mV/s (**Figure 7a**). The onset potentials corresponding to methanol for Pd/C, Pt/C, Pd/WO$_3$, and PdP/WO$_3$ are estimated to be 0.56, 0.54, 0.55, and 0.54 V, respectively. The methanol oxidation peak current measured for PdP/WO$_3$ is highest at 0.734 A mg^{-1} compared to 0.615 A mg^{-1} for Pd/C, 0.590 A mg^{-1} for Pt/C, and 0.505 A mg^{-1} for Pd/WO$_3$. The extracted values of the peak current density and peak current potential corresponding to the different catalysts employed are compiled in **Table 1**. A plot representing the experimental error corresponding to the peak current density of different catalysts employed is shown in **Figure S12**.The superior performance displayed by PdP/WO$_3$ in terms of both the peak current density and peak current potential can be explained by the electronic modification of the d-band of Pd brought in by the tensile strain induced in the Pd lattice as revealed by both the XRD and XPS analyses.[31] In addition to the d-band modification, P-doping in Pd creates lower coordination sites (defects, kinks, and edges), which also expects to be contributing towards the high catalytic activity. The P in the catalyst is present in the oxidized form as evident from the XPS results detailed in a previous section, which tends to provide necessary -OH species to oxidize the carbonaceous species.[55] Thus, this controlled interplay helps the Pd to effectively oxidize CO (a reaction intermediate) to CO$_2$, thereby making PdP/WO$_3$ a more CO tolerant system. Moreover, the absorbed OH species present on the metal oxide acts as a source of oxygen to the carbonaceous species in facilitating their oxidation.[37,12,56] Thus, coexistence of multiple favoring factors in the case of PdP/WO$_3$ makes it a more effective methanol oxidation catalyst with improved CO tolerance.

When molar concentration of the KOH was increased from 0.1 M to 1.0 M, increase in the peak current density with a concomitant negative shift in the peak potential has been observed (Figure 7.d). This enhancement in the activity can be explained in terms of the increased amount of OH$^-$ species.[57] Further, to confirm the stability of PdP/WO$_3$ for the methanol oxidation, potential cycling was performed in the region of 0 to 1.25 V. The peak current density is found to be decreased from 0.734 A mg^{-1} to 0.700 A mg^{-1} before and after the 100 potential cycling, respectively, compared to the drop from 0.590 A mg^{-1} to 0.501 A mg$_{Pt}^{-1}$ observed in the case of Pt/C (**Figure S13**). This further points towards the enhanced stability of PdP/WO$_3$ towards methanol oxidation. Further, long-term stability test of PdP/WO$_3$ was carried out by potential cycling between 0.0 to 1.2 V for 1000 cycles (**Figure S14**). A 10.6 % decrement in the activity has been observed after the potential cycling.

To verify the anti-CO poisoning performance during MOR, we have carried out the methanol oxidation on……in the presence and absence of CO saturated 0.1 M KOH and 1.0 M methanol. The positive shift in onset potential for the methanol oxidation is observed in CO saturated environment compared to the N$_2$ saturated one (**Figure….**). The onset potential is positively shifted by around ~ 0.25 V. The positive shift in the onset potential can be explained in terms of the active site blockage by CO adsorption. As we sweep more toward the positive potential during the forward cycling, the absorbed CO gets oxidized from the Pd surface. Hence, after a potential of ~0.80-0.85 V, we observed the same peak current density as observed in the N$_2$ saturated environment. This indicates the possibility that there is no CO poisoning happens during the methanol oxidation. However, the exact mechanism has to

understand through more focused and advanced investigation technologies.

   Recently, the ratio of the forward peak current (I_f) and the backward peak current (I_b) has been revised through the through a detailed in-situ surface-enhanced IR absorption spectroscopy (SEIRAS) study of the MOR.[58] So, accordingly, I_f and I_b shares the same chemical signature, i.e., the electrochemical oxidation of the methanol during the forward scanning and backward scanning.[59] Also, ratio of the forward peak current (I_f) and the backward peak current (I_b) can be used to define the oxophilic nature of the catalyst (Pt).[60] Also, it has been shown in the case of Pd that the CO oxidation takes place in the same potential region of the methanol oxidation.[61] This suggests that in addition to the methanol oxidation for the forward peak, the backward peak is also an indicative of the methanol oxidation. Thus, a high ratio of the forward peak current (I_f) to the backward peak current (I_b) has been correlated to the oxophilic nature of the Pd/Pt catalysts. [61,58] As the surface becomes more oxidized during the forward scan, it becomes more inactive for the oxidation of methanol during backward scanning. I_f/I_b values for PdP/WO$_3$ and Pd/WO$_3$ are 0.905 and 0.798 (**Figure 7b**, respectively, which are lower than that measured for Pd/C. Moreover, the backward peak for PdP/WO$_3$ for methanol oxidation appears at ~ 0.80 V while that for Pd/C appears at ~ 0.70 V (**Figure 7a**). This signifies the surface modification or change in the oxophilic character of the Pd anchored over WO$_3$ compared that decorated over carbon. This is further validated by the shift in the oxidation peaks of Pd-O in PdP/WO$_3$ compared to that in Pd/C, as evident from **Figure 7c**. This shows that in case of PdP/WO$_3$, the reduction of the Pd-O starts occurring at higher potential region, generating more surface for the methanol oxidation, therefore generating more current during the backward scan compared to the Pd supported over carbon.
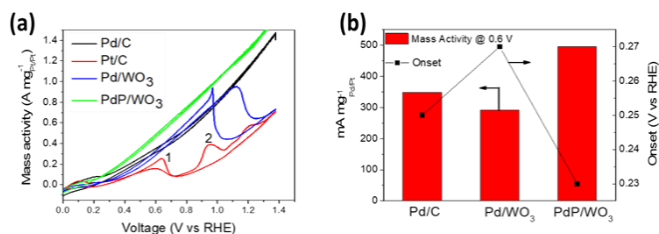

Figure 8. (a) CV profiles recorded for the formate oxidation for the various catalysts recorded in 0.1 M HCOOH + 0.3 M KOH and (b) comparison of the mass activity measured at 0.60 V and the onset potential recorded for the different catalysts.

   Apart from the ORR and methanol oxidation activity, PdP/WO$_3$ is also highly active and efficient for the formate oxidation; the electrochemical properties of the different catalysts for formate oxidation measured in 0.1 M HCOOH+ 0.3 M KOH electrolyte are presented in **Figure 8.** In alkaline medium, the formic acid gets deprotonated to form the formate ion (HCOO$^-$), which acts as the main oxidizing species. Mechanistic insight of the formate oxidation shows that the formate oxidation occurs through dual pathway namely the "Indirect Pathway" in which CO is an intermediate, and the "Direct Pathway" where formate is directly converted into CO$_2$ without the formation of the reaction intermediates; the two pathways are given below:[62]

Indirect Pathway (1):

$$HCOO^- \rightarrow HCOO_{(ads)} \rightarrow CO_{(ads)} \rightarrow CO_3^{2-}$$
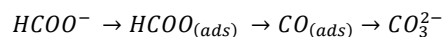
Direct Pathway (2):

$$HCOO^- \rightarrow HCOO_{(ads)} \rightarrow CO_3^{2-}$$

The direct pathway is favorable as it does not involve the CO intermediate which could poison the metal surface. Pd is the most effective catalyst for the formate oxidation because it follows the "Direct Pathway" mechanism. *Zhang et.al*, performed DFT calculations to examine the Pd –alloy catalyst for formate oxidation. Their study revealed that FOR prefers the direct dissociative pathway from a kinetic point of view, and the direct dissociative pathway from the thermodynamic point of view.[63] Also, the mechanistic origin of the formate oxidation on Pd/C has been studied using H/D kinetic isotope effect studies and electrochemical experiments. It has been revealed that formate oxidation to CO$_2$ occurs through a direct pathway.[64] On the other hand, the reaction on the Pt surface proceeds *via* the "Direct" as well as the "Indirect Pathway". Therefore, the Pt surface is easily blocked by the strongly adsorbed CO species.[65] In the case of the CV profiles recorded in the present case **(Figure 8a),** the lowest formate oxidation activity has been measured for Pt/C among all the catalysts. In **Figure 8a**, Peak 1 represented at ~ 0.56 V for Pt/C corresponds to the "Direct" oxidation of formate at the Pt sites while Peak 2 represented at ~ 0.90 V corresponds to both the "Direct" and "Indirect" pathways of the formate oxidation, in which the active surface is blocked by the strongly adsorbed CO species.[66] **Figure 8a** also points towards the better formate oxidation ability achievable on PdP/WO$_3$ compared to the counterpart systems namely Pd/C and Pd/WO$_3$ as evident from the low onset potential and high peak current obtained in the former case. The values of the onset potential and mass activity measured at 0.60 V equated for the different catalysts for the formate oxidation are presented in **Figure 8b**. **Figure S16** represents the experimental error in the measurement of the different catalysts at a potential of 0.60 V for formate oxidation.

Among the systems, PdP/WO$_3$ shows the highest value for the mass activity of nearly 0.50 A mg$_{Pd}^{-1}$, which conforms with the more favorable onset potential. Phosphorous doping in the Pd lattice is known to create structural distortions. Due to this structural disorder, there are more accessible reactive sites with low coordination numbers. Defects, kinks, and edges represent such low coordination sites, and these low coordinated atomic centers are the highly active locations for facilitating the reaction.[67] Also, P incorporation enhances the dispersion of the Pd nanoparticles and inhibits their aggregation. This further leads to a much more enhanced electro-catalytic performance of PdP/WO$_3$ for formate oxidation.[29] While, in the case of Pd/WO$_3$, agglomerated Pd particles having lower ECSA are formed compared to PdP/WO$_3$ and Pd/C, and also fewer defects due to the absence of P. This results into the low formate oxidation activity of Pd/WO$_3$.

During the formate oxidation, the hydrogen adsorption usually occurs on the Pd surface, which can inadvertently reduce the number of the active sites.[2] However, in the case of the WO$_3$ supported Pd nanoparticles, hydrogen spillover[68] may clean the Pd surface and regenerate the active sites in the process for the formate oxidation. Presumably, in the operating potential window, the surface blockage due to oxide formation is not sufficient to deactivate the formate oxidation in the case of PdP/WO$_3$ and Pd/C.[69] Also, oxidation of the Pd surface and oxidation of the formate/methanol over Pd are the

two competitive processes.[70] However, oxidation of the formate takes place much faster than the surface oxidation of the Pd within the potential range making Pd a highly active catalyst for the formate/methanol oxidation.

We have carried out a study to understand the CO poisoning effect during the formate oxidation reaction by recording the voltammograms in CO saturated 0.3 M KOH and ~ 0.1 M formic acid and in the absence of CO in the reaction medium. In the case of the CO saturated environment, the site blockage by the CO adsorption is expected to reduce the formate adsorption on the active centers. This lead to a peak due to PdO formation. During the backward scanning in CO saturated environment, the PdO gets reduced and Pd becomes free from the adsorbed CO. Hence, a sudden high current density is observed due to the formate oxidation during the backward scanning (**Figure S17**). While in the case of the CO-free environment, the formate oxidation occurs at a greater pace than that of the Pd surface oxidation; thus, no peak is observed due to the PdO formation.[70] Therefore, no mass-transfer issue associated with formate oxidation in the N_2 saturated environment occurs.

Further long term durability study of PdP/WO$_3$ was carried out by subjecting potential cycling between 0.0 to 0.80 V for 1000 cycles (**Figure S18**). A 12.7 % decrement in the activity has been observed after the test, which points towards better structural endurance and activity retention by the system.

Conclusion: We have developed a multi-functional material, PdP/WO$_3$, in which P-doped Pd nanoparticles are supported on the WO$_3$ nanorods. PdP/WO$_3$ shows excellent activity for oxygen reduction, methanol oxidation, and formate oxidation reactions. Moreover, PdP/WO$_3$ shows high stability and corrosion resistance at high potentials, retaining sixteen times higher activity than the *state-of-the-art* Pt/C for ORR after 3000 potential cycles swept at a high scan rate. Also, the electronic structure of the Pd nanoparticles could be successfully modified by doping P in the Pd lattice; P-doping induces tensile strain which along with SMSI modulates the activity of Pd. Consequently, the highest activity for the formate and methanol oxidation could be achieved on the PdP/WO$_3$. The study confirms that the addition of the P in Pd lattice and using WO$_3$ as the support material have a significant beneficial effect on favorably modulating the electrochemical activity of the Pd. This advantage makes PdP/WO$_3$ as a versatile multi-functional catalyst which can be used in the liquid fuel cells as the anode catalyst for the formic acid oxidation and methanol oxidation as well as the cathode catalyst for facilitating oxygen reduction. Thus, this work will make notable contributions towards the development of efficient and cost-effective carbon-free electrocatalysts for fuel cells. Moreover, as a future prospective, since CO_3^{2-} generated in the direct liquid fuel cells can be further converted to formate/formic acid and methanol using CO_2 electrolyzer and chemical routes, the generation of carbon footprints can be mitigated, which also sorts out the issue associated with the cost of manufacturing.

Notes

The authors declare no competing financial interest

References

1   X. Liang, B. Liu, J. Zhang, S. Lu and Z. Zhuang, *Chemical Communications*, 2016, **52**, 11143–11146.

2   S. Sankar, G. M. Anilkumar, T. Tamaki and T. Yamaguchi, *ACS Applied Energy Materials*, 2018, **1**, 4140–4149.

3   A. Klinkova, P. De Luna, E. H. Sargent, E. Kumacheva and P. V. Cherepanov, *Journal of Materials Chemistry A*, 2017, **5**, 11582–11585.

4   Z. Cui, M. Yang and F. J. Disalvo, *Mesoporous Ti0.5Cr0.5N supported PdAg nanoalloy as highly active and stable catalysts for the electro-oxidation of formic acid and methanol*, 2014, vol. 8.

5   C. Lafforgue, F. Maillard, V. Martin, L. Dubau and M. Chatenet, *ACS Catalysis*, 2019, 5613–5622.

6   Z. Awaludin, J. G. Sheng Moo, T. Okajima and T. Ohsaka, *Journal of Materials Chemistry A*, 2013, **1**, 14754–14765.

7   B. Liu, J. Liu, T. Li, Z. Zhao, X. Q. Gong, Y. Chen, A. Duan, G. Jiang and Y. Wei, *Journal of Physical Chemistry C*, 2015, **119**, 12923–12934.

8   L. Ye, A. H. Mahadi, C. Saengruengrit, J. Qu, F. Xu, S. M. Fairclough, N. Young, P. L. Ho, J. Shan, L. Nguyen, F. F. Tao, K. Tedsree and S. C. E. Tsang, *ACS Catalysis*, 2019, **9**, 5171–5177.

9   M. L. Hernández-Pichardo, R. G. González-Huerta, P. Del Angel, M. Tufiño-Velazquez and L. Lartundo, *International Journal of Hydrogen Energy*, 2015, **40**, 17371–17379.

10   Z. Xi, J. Li, D. Su, M. Muzzio, C. Yu, Q. Li and S. Sun, *Journal of the American Chemical Society*, 2017, **139**, 15191–15196.

11   Z. Xi, D. P. Erdosy, A. Mendoza-Garcia, P. N. Duchesne, J. Li, M. Muzzio, Q. Li, P. Zhang and S. Sun, *Nano Letters*, 2017, **17**, 2727–2731.

12   J. Mateos-Santiago, M. L. Hernández-Pichardo, L. Lartundo-Rojas and A. Manzo-Robledo, *Industrial and Engineering Chemistry Research*, 2017, **56**, 161–167.

13   J. Wang, Z. Wang and C. J. Liu, *ACS Applied Materials and Interfaces*, 2014, **6**, 12860–12867.

14   Q. Zhang, X. X. Qin, F. P. Duan-Mu, H. M. Ji, Z. R. Shen, X. P. Han and W. Bin Hu, *Angewandte Chemie - International Edition*, 2018, **57**, 9351–9356.

15   C. Yang, M. Zhou, M. Zhang and L. Gao, *Electrochimica Acta*, 2016, **188**, 529–536.

16   Y. Lu, Y. Jiang, X. Gao, X. Wang and W. Chen, *Journal of the American Chemical Society*, 2014, **136**, 11687–11697.

17   S. R. Chowdhury and T. Maiyalagan, *International Journal of Hydrogen Energy*, 2019, **44**, 14808–14819.

18   J. Xue, G. Han, W. Ye, Y. Sang, H. Li, P. Guo and X. S. Zhao, *ACS Applied Materials and Interfaces*, 2016, **8**, 34497–34505.

19   L. Zhang, Y. Tang, J. Bao, T. Lu and C. Li, *Journal of Power Sources*, 2006, **162**, 177–179.

20   Y. Xie, W. Yu, J. Wang, Y. Wu, S. Niu, W. Guo, T. Lin and L. Shao, *Physical Chemistry Chemical Physics*, 2017, **19**, 25214–25219.

13

21   D. Chai, W. Wang, W. Dong, Y. Kang, Y. Dong and Z. Lei, *Applied Catalysis A: General*, 2016, **525**, 1–8.

22   J. Zhang, Y. Xu and B. Zhang, *Chemical Communications*, 2014, **50**, 13451–13453.

23   K. C. Poon, D. C. L. Tan, T. D. T. Vo, B. Khezri, H. Su, R. D. Webster and H. Sato, *Journal of the American Chemical Society*, 2014, **136**, 5217–5220.

24   L. Cheng, Z. Zhang, W. Niu, G. Xu and L. Zhu, *Journal of Power Sources*, 2008, **182**, 91–94.

25   K. C. Poon, D. C. L. Tan, T. D. T. Vo, B. Khezri, H. Su, R. D. Webster and H. Sato, *Newly developed stepwise electroless deposition enables a remarkably facile synthesis of highly active and stable amorphous Pd nanoparticle electrocatalysts for oxygen reduction reaction*, 2014, vol. 136.

26   J. Wang, E. Khoo, P. S. Lee and J. Ma, *Journal of Physical Chemistry C*, 2009, **113**, 9655–9658.

27   J. Diao, W. Yuan, Y. Qiu, L. Cheng and X. Guo, *Journal of Materials Chemistry A*, 2019, **7**, 6730–6739.

28   H. Xu, B. Yan, K. Zhang, C. Wang, J. Zhong, S. Li, P. Yang and Y. Du, *International Journal of Hydrogen Energy*, 2017, **42**, 11229–11238.

29   L. Cheng, Z. Zhang, W. Niu, G. Xu and L. Zhu, *Journal of Power Sources*, 2008, **182**, 91–94.

30   L. Wang, J. J. Zhai, K. Jiang, J. Q. Wang and W. Bin Cai, *International Journal of Hydrogen Energy*, 2015, **40**, 1726–1734.

31   V. Celorrio, P. M. Quaino, E. Santos, J. Flórez-Montaño, J. J. L. Humphrey, O. Guillén-Villafuerte, D. Plana, M. J. Lázaro, E. Pastor and D. J. Fermín, *ACS Catalysis*, 2017, **7**, 1673–1680.

32   W. Zhou and J. Y. Lee, *Journal of Physical Chemistry C*, 2008, **112**, 3789–3793.

33   M. Li, Z. Zhao, T. Cheng, A. Fortunelli, C. Y. Chen, R. Yu, Q. Zhang, L. Gu, B. V. Merinov, Z. Lin, E. Zhu, T. Yu, Q. Jia, J. Guo, L. Zhang, W. A. Goddard, Y. Huang and X. Duan, *Science*, 2016, **354**, 1414–1419.

34   L. Zhang, L. Wan, Y. Ma, Y. Chen, Y. Zhou, Y. Tang and T. Lu, *Applied Catalysis B: Environmental*, 2013, **138**–**139**, 229–235.

35   M. Gong, Z. Deng, D. Xiao, L. Han, T. Zhao, Y. Lu, T. Shen, X. Liu, R. Lin, T. Huang, G. Zhou, H. Xin and D. Wang, *ACS Catalysis*, 2019, **9**, 4488–4494.

36   S. Kumar, S. N. Bhange, R. Soni and S. Kurungot, *ACS Applied Energy Materials*, 2020, **3**, 1908–1921.

37   E. A. Monyoncho, S. Ntais, N. Brazeau, J. J. Wu, C. L. Sun and E. A. Baranova, *ChemElectroChem*, 2016, **3**, 218–227.

38   L. Chen, L. Lu, H. Zhu, Y. Chen, Y. Huang, Y. Li and L. Wang, *Nature Communications*, , DOI:10.1038/ncomms14136.

39   T. T. Vo Doan, J. Wang, K. C. Poon, D. C. L. Tan, B. Khezri, R. D. Webster, H. Su and H. Sato, *Angewandte Chemie - International Edition*, 2016, **55**, 6842–6847.

40   G. Cui, S. Song, P. K. Shen, A. Kowal and C. Bianchini, *Journal of Physical Chemistry C*, 2009, **113**, 15639–15642.

41   H. Xin and S. Linic, *Journal of Chemical Physics*, , DOI:10.1063/1.3437609.

42   J. Li, H. Zhou, H. Zhuo, Z. Wei, G. Zhuang, X. Zhong, S. Deng, X. Li and J. Wang, *Journal of Materials Chemistry A*, 2018, **6**, 2264–2272.

43   L. Chen, H. Guo, T. Fujita, A. Hirata, W. Zhang, A. Inoue and M. Chen, *Advanced Functional Materials*, 2011, **21**, 4364–4370.

44   S. Fu, C. Zhu, D. Du and Y. Lin, *ACS Applied Materials and Interfaces*, 2015, **7**, 13842–13848.

45   L. Zhang and G. Henkelman, *Journal of Physical Chemistry C*, 2012, **116**, 20860–20865.

46   C. Wang, L. Zheng, R. Chang, L. Du, C. Zhu, D. Geng and D. Yang, *ACS Applied Materials and Interfaces*, 2018, **10**, 29965–29971.

47   J. Yue, Z. Du and M. Shao, *Journal of Physical Chemistry Letters*, 2015, **6**, 3346–3351.

48   D. Wang, H. L. Xin, R. Hovden, H. Wang, Y. Yu, D. A. Muller, F. J. Disalvo and H. D. Abruña, *Nature Materials*, 2013, **12**, 81–87.

49   J. Parrondo, T. Han, E. Niangar, C. Wang, N. Dale, K. Adjemian and V. Ramani, *Proceedings of the National Academy of Sciences of the United States of America*, 2014, **111**, 45–50.

50   A. Zadick, L. Dubau, N. Sergent, G. Berthomé and M. Chatenet, *ACS Catalysis*, 2015, **5**, 4819–4824.

51   C. Lafforgue, F. Maillard, V. Martin, L. Dubau and M. Chatenet, *ACS Catalysis*, 2019, 5613–5622.

52   D. R. Lide and G. Baysinger, *Choice Reviews Online*, 2004, **41**, 41-4368-41–4368.

53   Y. Garsany, O. A. Baturina, K. E. Swider-Lyons and S. S. Kocha, *Analytical Chemistry*, 2010, **82**, 6321–6328.

54   J. Zhang, Y. Xu and B. Zhang, *Chemical Communications*, 2014, **50**, 13451–13453.

55   H. Lv, D. Xu, L. Sun, J. Henzie, S. L. Suib, Y. Yamauchi and B. Liu, *Ternary palladium-boron-phosphorus alloy mesoporous nanospheres for highly efficient electrocatalysis*, 2019, vol. 13.

56   S. Yoon, K. Oh, F. Liu, J. H. Seo, G. A. Somorjai, J. H. Lee and K. An, *ACS Catalysis*, 2018, **8**, 5391–5398.

57   S. Yan, S. Zhang, Y. Lin and G. Liu, *Journal of Physical Chemistry C*, 2011, **115**, 6986–6993.

58   A. M. Hofstead-Duffy, D. J. Chen, S. G. Sun and Y. J. Tong, *Journal of Materials Chemistry*, 2012, **22**, 5205–5208.

59   J. Li, S. Z. Jilani, H. Lin, X. Liu, K. Wei, Y. Jia, P. Zhang, M. Chi, Y. Y. J. Tong, Z. Xi and S. Sun, *Angewandte Chemie - International Edition*, 2019, **58**, 11527–11533.

60   D. Y. Chung, K. J. Lee and Y. E. Sung, *Journal of Physical Chemistry C*, 2016, **120**, 9028–9035.

61   C. H. W. Kelly, T. M. Benedetti, A. Alinezhad, W. Schuhmann, J. J. Gooding and R. D. Tilley, *Journal of Physical Chemistry C*, 2018, **122**, 21718–21723.

62   A. O. Elnabawy, J. A. Herron, J. Scaranto and M. Mavrikakis, *Journal of The Electrochemical Society*, 2018, **165**, J3109–J3121.

63   N. Zhang, F. Chen and L. Guo, *Physical Chemistry Chemical Physics*, 2019, **21**, 22598–22610.

64   M. Choun, S. Hong and J. Lee, *Journal of The Electrochemical Society*, 2018, **165**, J3266–J3270.

65   Z. Cui, M. Yang and F. J. Disalvo, *ACS Nano*, 2014, **8**, 6106–6113.

66   J. John, H. Wang, E. D. Rus and H. D. Abruña, *Journal of Physical Chemistry C*, 2012, **116**, 5810–5820.

67   K. C. Poon, D. C. L. Tan, T. D. T. Vo, B. Khezri, H. Su, R. D. Webster and H. Sato, *Journal of the American Chemical Society*, 2014, **136**, 5217–5220.

68   W. L. Qu, Z. B. Wang, Y. Gao, C. Deng, R. H. Wang, L. Zhao and X. L. Sui, *International Journal of Hydrogen Energy*, 2018, **43**, 407–416.

69   J. Noborikawa, J. Lau, J. Ta, S. Hu, L. Scudiero, S. Derakhshan, S. Ha and J. L. Haan, *Electrochimica Acta*, 2014, **137**, 654–660.

70   X. Li, H. Hodson, C. Batchelor-Mcauley, L. Shao and R. G. Compton, *ACS Catalysis*, 2016, **6**, 7118–7124.